

# The Emission due to the Interaction of a Poynting Jet and the Ejecta

Ning-Yuan Zhang, Yun-Peng Li<sup>1</sup>, Bo-Song Qin, Yu-Fei Li, and Da-Bin Lin<sup>1</sup>
Guangxi Key Laboratory for Relativistic Astrophysics, School of Physical Science and Technology, Guangxi University, Nanning 530004, China; lypzhw@st.gxu.edu.cn, lindabin@gxu.edu.cn

Received 2025 July 10; revised 2025 September 20; accepted 2025 October 1; published 2025 November 13

#### **Abstract**

The merger of two neutron stars may lead to the formation of a rapidly rotating magnetar. The interaction between the Poynting-flux-dominated jet and the surrounding ejecta gives rise to a pulsar wind nebula, which produces multi-band electromagnetic emission. Unlike previous models that assume constant jet properties, we incorporate the radial evolution of the jet magnetization parameter ( $\sigma$ ) and Lorentz factor, where  $\sigma$  decreases and the Lorentz factor increases with radius due to magnetic dissipation. We solve the coupled dynamics of the forward shock (FS), reverse shock (RS), and contact discontinuity (CD), and find that a large ejecta mass ( $M_{\rm ej} > 3 \times 10^{-4} \, M_{\odot}$ ) leads to the rapid inward propagation and eventual disappearance of the RS. For smaller ejecta masses, distinct dynamical phases are identified: an initially backward-propagating RS, a prolonged lag of the RS behind the FS and CD during ejecta traversal, and a final convergence after the FS emerges into the interstellar medium. The emission evolves correspondingly, appearing as blackbody radiation from the optically thick ejecta at early times, and later transitioning to synchrotron and external inverse Compton emission from the RS once the system becomes optically thin.

Key words: (stars:) gamma-ray burst: general – stars: magnetars – (stars:) pulsars: general

## 1. Introduction

The merger of binary neutron stars (BNS) represents a major astrophysical event that provides valuable insights into high-energy astrophysics, gravitational wave astronomy, and the formation of heavy elements. In a BNS merger, two neutron stars orbit each other and gradually lose energy due to gravitational radiation, spiraling closer together until they finally collide and merge. The observation of gravitational waves from such mergers was first achieved in 2017 with the detection of GW170817, a landmark event observed by LIGO and Virgo (Harry & LIGO Scientific Collaboration 2010; Somiya 2012; Bartos et al. 2013; Acernese et al. 2015; Abbott et al. 2017a, 2017b). This event confirmed that neutron star mergers are sources of gravitational waves and provided compelling evidence linking them to short gamma-ray bursts (sGRBs) and kilonova emissions associated with the production of heavy elements via rapid neutron capture (r-process) (Li & Paczyński 1998). The remnant formed after the merger depends on factors such as the masses and spins of the initial neutron stars (Paczynski 1986; Eichler et al. 1989; Barthelmy et al. 2005; Fox et al. 2005; Rezzolla et al. 2011; Li et al. 2024). It may collapse promptly into a black hole or form a hypermassive or even a stable neutron star. In the latter case, the remnant can be a rapidly rotating, highly magnetized object

known as a millisecond magnetar (Dai et al. 2006; Zhang 2013).

The formation of a magnetar can power relativistic outflows that contribute to the prompt gamma-ray burst emission and influence the subsequent multi-wavelength afterglow observed in X-ray, optical, and radio bands (Dai et al. 2006; Rowlinson et al. 2010, 2013; Dai & Liu 2012; Wang & Dai 2013; Gompertz et al. 2014; Gao et al. 2015). Recent studies have systematically investigated the electromagnetic signatures powered by post-merger magnetars to identify their formation in BNS or neutron star-black hole (NS-BH) mergers (Gao et al. 2013; Wang & Dai 2013; Yu et al. 2013, 2015; Zhang 2013; Gompertz et al. 2014; Wu et al. 2014; Wang et al. 2015; Siegel & Ciolfi 2016a, 2016b; Li & Yu 2016; Li et al. 2025). In particular, these works focus on scenarios involving continuous energy injection into the surrounding ejecta (Dai & Lu 1998a, 1998b; Zhang & Mészáros 2001; Dai 2004), which can produce extended afterglows and flares in sGRB. Corresponding observations provide key constraints on the physical properties of magnetar-powered pulsar wind nebulae (PWN) and help unravel the complex dynamics of these high-energy transients.

A PWN is formed by the interaction between the pulsar wind and the surrounding ejecta, and typically consists of the following structures (Kotera et al. 2013): a forward shock (FS) at the interface between the shocked and unshocked ejecta, and a reverse shock (RS) at the interface between the shocked and

<sup>&</sup>lt;sup>1</sup> Corresponding authors.

unshocked pulsar wind (commonly referred to as the "termination shock"). The region between these two shocks, composed of shocked material, constitutes the PWN (Chevalier & Fransson 1992; Gaensler & Slane 2006; Kotera et al. 2013). However, the evolution of the leptonic-matterdominated jet is often simplified in previous studies. Previous models usually assume that the physical properties of the jet remain uniform throughout. In reality, both the jet magnetization parameter  $(\sigma)$  and the Lorentz factor evolve with the radius. Specifically, as the radius increases, the magnetization parameter decreases while the Lorentz factor increases, deviating from the conventional assumption of constant  $\sigma$ and Lorentz factor. In addition, thermal photons from the ejecta may return to the PWN and serve as seed photons for external inverse Compton (EIC) scattering. In this study, we incorporate the evolution of the jet's magnetization parameter and Lorentz factor, and explore the role of thermal-photon IC scattering within the PWN. By accounting for these previously overlooked interactions, our work aims to provide a more complete understanding of the radiative processes occurring in post-merger magnetar PWNe, offering improved diagnostics of their multi-wavelength emission and potential insights into the late-time evolution of the ejecta.

This paper is organized as follows. In Section 2, we present our model for various radiation processes within the PWN, including synchrotron radiation and EIC. Section 3 describes the numerical results. Finally, conclusions and a discussion are provided in Section 4.

## 2. Model

If a BNS merger results in the formation of a highly magnetized, rapidly rotating NS (i.e., a magnetar) rather than a BH, it can launch a relativistic magnetar wind. This wind is initially dominated by Poynting flux, which is subsequently converted into a particle-dominated outflow composed primarily of electron-positron pairs at larger radii (Coroniti 1990; Michel 1994; Dai 2004; Yu & Dai 2007). As the relativistic wind interacts with the slower-moving ejecta, it is decelerated, leading to the formation of an RS and an FS. In Section 2.1, we present the spin-down luminosity of the magnetar and describe the dynamical evolution of the PWN. Section 2.2 provides calculations of the synchrotron radiation from the shocked region and the EIC process involving thermal photons originating from the ejecta and returning to the shocked region.

## 2.1. Ejecta Dynamics and the Reverse Shock

We assume that the merger of a BNS leads to the formation of a magnetar. The physical scenario adopted in this paper is illustrated in Figure 1 of Gao et al. (2013) and Figure 1 of Wang et al. (2015). The interaction between the magnetar wind and both the ejecta and the ambient medium gives rise to

a relativistic wind bubble (Dai 2004; Yu & Dai 2007; Mao et al. 2010; Wang & Dai 2013; Wang et al. 2015; Liu et al. 2016). Two shocks form in this scenario: an RS that propagates into the unshocked magnetar wind, and an FS that propagates into the ambient medium. Consequently, the relativistic wind bubble consists of four regions, separated by two shocks and a contact discontinuity (CD):

- 1. Region 1: the unshocked ambient medium;
- 2. Region 2: the forward-shocked ambient medium;
- 3. Region 3: the reverse-shocked magnetar wind;
- 4. Region 4: the unshocked magnetar wind.

Regions 2 and 3 are separated by a CD.

The spin-down luminosity of the magnetar formed after the BNS merger is given by (Duncan & Thompson 1992; Giacomazzo & Perna 2013):

$$L_{\rm sd} = \begin{cases} L_{\rm sd,0} \left( 1 + \frac{t_{\rm inj}}{t_{\rm sd}} \right)^{-\alpha_1}, & t_{\rm inj} \geqslant 0, \\ 0, & t_{\rm inj} < 0, \end{cases}$$
 (1)

where  $L_{\rm sd,0}=1\times 10^{52}~{\rm erg~s^{-1}}~B_{\rm p,15}^2R_{\rm s,6}^{~6}P_{\rm 0,-3}^{-4}$  is the initial spin-down luminosity, with  $B_{\rm p,15}=B_{\rm p}/10^{15}~{\rm G}$  the surface dipole magnetic field in units of  $10^{15}~{\rm G}$ ,  $R_{\rm s,6}=R_{\rm s}/10^{6}~{\rm cm}$  the NS radius in units of  $10^{6}~{\rm cm}$ , and  $P_{\rm 0,-3}=P_{\rm 0}/10^{-3}~{\rm s}$  the initial spin period in units of 1 ms. The injection time in the source frame is defined as  $t_{\rm inj}=(c\beta_{\rm jet}t+R_{\rm acc}-R_{\rm rs})/(c\beta_{\rm jet})$ , where  $R_{\rm acc}=1\times 10^{7}~{\rm cm}$  is the jet acceleration radius, and  $R_{\rm rs}$  is the radius of the reverse shock. The power-law index is  $\alpha_1=5/3$ , and the characteristic spin-down timescale is  $t_{\rm sd}=1\times 10^6~{\rm s}~I_{\rm s,45}B_{\rm p,15}^{-2}R_{\rm s,6}^{-6}P_{\rm 0,-3}^2$ , where  $I_{\rm s,45}=I_{\rm s}/10^{45}~{\rm g}~{\rm cm}^2$  is the moment of inertia of the magnetar in units of  $10^{45}~{\rm g}~{\rm cm}^2$ . For a typical millisecond magnetar, the dimensionless parameters  $I_{\rm s,45},~R_{\rm s,6},~{\rm and}~P_{\rm 0,-3}$  are all of order unity. Throughout this paper, we adopt the conventional notation  $Q=10^nQ_n$ .

After the formation of the relativistic stellar wind bubble, the total energy of the bubble in the progenitor frame is

$$E_{\text{tot}} = \Gamma_3 M_{0.3} c^2 + \Gamma_3 m c^2 + \Gamma_{\text{eff}} E'_{\text{int} 2} + \Gamma_{\text{eff}} E'_{\text{int} 3}.$$
 (2)

Energy conservation requires

$$dE_{\text{tot}} = dmc^2 + \Gamma_{\text{eff}} dE'_{\text{loss rad 2}} + \Gamma_{\text{eff}} dE'_{\text{loss rad 3}} + dE_{\text{sd}}. \quad (3)$$

Here,  $dE'_{\rm int,2} = (\Gamma_3 - 1)dmc^2 + dE'_{\rm ad,2} + dE'_{\rm loss,rad,2}$  and  $dE'_{\rm int,3} = (\Gamma_{34} - 1)f_a dM_{0,3}c^2 + dE'_{\rm ad,3} + dE'_{\rm loss,rad,3}$ , where the first term represents the random kinetic energy produced at the shock via inelastic collisions, the second term corresponds to the energy lost due to adiabatic expansion, and the third term denotes the radiative losses, given by  $dE'_{\rm loss,rad,2}$  and  $dE'_{\rm loss,rad,3}$  for Region 2 and Region 3, respectively.

The dynamical evolution can then be described as (Nava et al. 2013):

$$\frac{d\Gamma_{3}}{dR} = -\frac{(\Gamma_{\text{eff}} + 1)(\Gamma_{3} - 1)\frac{dm}{dR}c^{2} + (\Gamma_{3} - f_{a}\Gamma_{\text{eff}} + f_{a}\Gamma_{\text{eff}}\Gamma_{3}4)\frac{dM_{0,3}}{dR}c^{2} + \Gamma_{\text{eff}}\frac{dE'_{\text{ad},3}}{dR} + \Gamma_{\text{eff}}\frac{dE'_{\text{ad},2}}{dR} - \frac{dE_{\text{sd}}}{dR}}{(M_{0,3} + m)c^{2} + E'_{\text{int},2}\frac{\Gamma_{\text{eff}}}{\Gamma_{3}} + E'_{\text{int},3}\frac{\Gamma_{\text{eff}}}{\Gamma_{3}}}.$$
(4)

Here,  $\Gamma_3$  denotes the Lorentz factor of Region 3, which is equal to that of Region 2, i.e.,  $\Gamma_3 = \Gamma_2$ . The initial value is set to  $\Gamma_{3,0} = 1.1$ . The effective Lorentz factor is defined as  $\Gamma_{\rm eff} = (\hat{\gamma}\Gamma_3^2 - \hat{\gamma} + 1)/\Gamma_3$ , where  $\hat{\gamma} = (4 + \Gamma_3^{-1})/3$  is the adiabatic index in the relativistic regime. The relative Lorentz factor between the unshocked magnetar wind (Region 4) and the blast wave is given by  $\Gamma_{34} = \Gamma_4\Gamma_3(1 - \beta_4\beta_3)$ , where  $\Gamma_4$  is the Lorentz factor of Region 4, and  $\beta_4 = \sqrt{1 - 1/\Gamma_4^2}$  and  $\beta_3 = \sqrt{1 - 1/\Gamma_3^2}$  are the corresponding velocities in units of speed of light c. The evolution of the swept-up mass from the unshocked ambient medium by the FS as a function of radius is given by  $dm/dR = 4\pi R^2 \rho$ . Suppose that the unshocked ejecta has a wind-like density profile and that the FS eventually propagates into the outer interstellar medium (ISM), i.e.,

$$\rho(R) = \begin{cases} A_0 R^{-2}, & R_{\text{ejecta}}, \ 0 < R \leqslant R_{\text{fin}}, \\ n_{\text{ISM}} m_{\text{p}}, & R > R_{\text{fin}}, \end{cases}$$
(5)

where the initial radius of the ejecta is  $R_{\rm ejecta,0} = 5 \times 10^{10}$  cm and the outer radius is taken as  $R_{\rm fin} = 100 \, R_{\rm ejecta,0}$ . Here,  $n_{\rm ISM}$  is the number density of the ISM, assumed to have a fiducial value of  $0.1 \, {\rm cm}^{-3}$ , and  $A_0$  is the normalization constant determined by mass conservation,

$$\int_{R_{\text{ciccta}},0}^{R_{\text{fin}}} 4\pi R^2 \rho(R) dR = M_{\text{ejecta}}.$$
 (6)

Additionally, the energy injected into Region 3 by the spindown of the magnetar can be expressed as

$$\frac{dE_{\rm sd}}{dt} = L_{\rm sd} \frac{\beta_4 - \beta_{\rm rs}}{\beta_4}. (7)$$

The evolution of the mass in the RS magnetar wind region (Region 3) is given by

$$\frac{dM_{0,3}}{dR} = \frac{L_{\rm sd}}{c^3 \Gamma_4 (1+\sigma)} \frac{\beta_4 - \beta_{\rm rs}}{\beta_3 \beta_4},\tag{8}$$

where  $\sigma$  is the magnetization parameter of the wind. As the radius increases, magnetic energy in the jet is gradually dissipated and converted into kinetic energy, leading to a decrease in  $\sigma$  and an increase in  $\Gamma_4$ . The evolution of  $\sigma$  can be modeled as  $\sigma = (\Gamma_{4,\text{max}}/\Gamma_4)^{2/3}$  (Drenkhahn & Spruit 2002), where  $\Gamma_{4,\text{max}} = \sigma_0^{3/2}$  is the maximum achievable Lorentz factor of Region 4, and  $\sigma_0 = 100$  is the initial magnetization parameter. Following Beniamini & Giannios (2017), the radial

evolution of  $\Gamma_4$  is given by

$$\Gamma_{4} = \begin{cases} \Gamma_{4,\max} \left( \frac{R_{fs}}{R_{satu}} \right)^{1/3}, & R_{acc} < R_{rs} \leqslant R_{satu}, \\ \Gamma_{4,\max}, & R_{rs} > R_{satu}, \end{cases}$$
(9)

where  $R_{\rm fs}$  is the radius of the FS, and  $R_{\rm satu}$  is the saturation radius of the magnetar wind, given by  $R_{\rm satu} = R_{\rm acc} \Gamma_{4,\rm max}^3$  (Drenkhahn & Spruit 2002).

The internal energy and adiabatic loss in Region 2 can be expressed as (Nava et al. 2013)

$$E'_{\text{int},2}(R) = c^2 \int_0^R \{ dm(r_{\text{fs}}) \mu_p [\gamma_{\text{ad,p,2}}(R, r) - 1] + dm(r_{\text{fs}}) \mu_e [\gamma_{\text{ad,e,2}}(R, r) - 1] \},$$
 (10)

and

$$\frac{dE'_{\text{ad},2}(R)}{dR} = -c^2 \left( \frac{1}{R} - \frac{1}{3} \frac{d \log \Gamma_3}{dR} \right) 
\times \int_0^R \left[ dm(r_{\text{fs}}) \mu_p \frac{p_{\text{ad},p,2}^2(R,r)}{\gamma_{\text{ad},p,2}(R,r)} + dm(r_{\text{fs}}) \mu_e \frac{p_{\text{ad},e,2}^2(R,r)}{\gamma_{\text{ad},e,2}(R,r)} \right],$$
(11)

respectively. Due to adiabatic expansion, the Lorentz factors of post-shock protons and electrons decrease over time. Their values at the current radius R are given by  $\gamma_{\rm ad,p,2} = \sqrt{p_{\rm ad,p,2}^2 + 1}$  and  $\gamma_{\rm ad,e,2} = \sqrt{p_{\rm ad,e,2}^2 + 1}$ , where  $p_{\rm ad,p,2}$  and  $p_{\rm ad,e,2}$  are the comoving momenta at R.

For a particle injected at shock radius r with initial momentum p(r), the comoving momentum at radius R is

$$p_{\text{ad,p,2}}(R, r) = \frac{r_{\text{rs}}}{r_{\text{rs}} + R_{\text{cd}} - r_{\text{cd}}} \times \left[ \frac{\Gamma(R)}{\Gamma(r)} \right]^{1/2} [\gamma_{\text{acc,p,2}}^2(r) - 1]^{1/2}, \quad (12)$$

$$p_{\text{ad,e,2}}(R, r) = \frac{r_{\text{rs}}}{r_{\text{rs}} + R_{\text{cd}} - r_{\text{cd}}} \times \left[\frac{\Gamma(R)}{\Gamma(r)}\right]^{1/2} [\gamma_{\text{rad,e,2}}^2(r) - 1]^{1/2}.$$
 (13)

The mean Lorentz factors of freshly shocked protons and electrons at injection radius r are given by

$$\gamma_{\text{acc},p,2}(r) = \left[\Gamma(r) - 1\right] \frac{\epsilon_{\text{p}}}{\mu_{\text{p}}} + 1, \tag{14}$$

$$\gamma_{\text{rad,e,2}}(r) = (1 - \epsilon_{\text{rad}})[\Gamma(r) - 1)] \frac{\epsilon_{\text{e}}}{\mu_{\text{e}}} + 1.$$
 (15)

Here,  $\epsilon_{\rm rad}$  denotes the fraction of the energy carried by electrons that is lost to radiation, while  $\epsilon_{\rm p}$  and  $\epsilon_{\rm e}$  represent the fractions of the total dissipated energy transferred to protons and electrons, respectively. The parameter  $\mu_{\rm p}=\rho_{\rm p}/\rho$  denotes the mass density fraction of shocked protons relative to the total shocked mass density, and is typically approximated as  $\mu_{\rm p} \simeq 1$ . Similarly,  $\mu_{\rm e}=\rho_{\rm e}/\rho$  denotes the mass density fraction of shocked electrons and positrons (hereafter simply referred to as "electrons"). In the absence of electron-positron pairs, electrons and protons have the same number density and identical radial profiles, leading to  $\mu_{\rm e} \simeq m_{\rm e}/m_{\rm p}$ .

Similarly, the internal energy and adiabatic loss in Region 3 can be written as (Nava et al. 2013)

$$E'_{\text{int,3}}(R_{\text{cd}}) = c^2 \int_0^R \{ dM_{0,3}(r_{\text{rs}}) \mu_{\text{p}}[\gamma_{\text{ad,p,3}}(R, r) - 1] + dM_{0,3}(r_{\text{rs}}) \mu_{\text{e}}[\gamma_{\text{ad,e,3}}(R, r) - 1] \},$$
 (16)

and

$$\frac{dE'_{\text{ad},3}(R_{\text{cd}})}{dR_{\text{cd}}} = -c^2 \left( \frac{1}{R_{\text{cd}}} - \frac{1}{3} \frac{d \log \Gamma_3}{dR_{\text{cd}}} \right) \\
\times \int_0^R \left[ dM_{0,3}(r_{\text{rs}}) \mu_{\text{p}} \frac{p_{\text{ad},p,3}^2(R,r)}{\gamma_{\text{ad},p,3}(R,r)} + dM_{0,3}(r_{\text{rs}}) \mu_{\text{e}} \frac{p_{\text{ad},e,3}^2(R,r)}{\gamma_{\text{ad},e,3}(R,r)} \right], \tag{17}$$

respectively. The calculation of adiabatic quantities in Region 3 follows the same method as for Region 2. However, since the magnetization parameter  $\sigma>0$  in Region 3, the mean post-shock Lorentz factors for protons and electrons are modified to

$$\gamma_{\text{acc},p,3} = f_{a} (\Gamma_{34} - 1) \frac{\epsilon_{p}}{\mu_{p}} + 1,$$
 (18)

$$\gamma_{\text{rad,e,3}} = f_{\text{a}} (1 - \epsilon_{\text{rad}}) (\Gamma_{34} - 1) \frac{\epsilon_{\text{e}}}{\mu_{\text{e}}} + 1,$$
 (19)

where the magnetization correction factor  $f_a$  is given by (Zhang & Kobayashi 2005; Mao et al. 2010)

$$f_{\rm a} \approx 1 - \frac{\sigma}{2u_{3s}^2 + 2u_{3s}\sqrt{u_{3s} + 1}},$$
 (20)

and the downstream four-velocity  $u_{3s}$  satisfies the quartic equation:

$$8(\sigma+1)u_{3s}^4 - (8\sigma^2 + 10\sigma + 1)u_{3s}^2 + \sigma^2 = 0,$$
 (21)

as derived in Fan et al. (2004) and Zhang & Kobayashi (2005).

The evolution of the FS, RS, and CD radii is governed by the velocities of the respective regions:

$$\frac{dR_{\rm fs}}{dt} = \beta_{\rm fs}c, \quad \frac{dR_{\rm rs}}{dt} = \beta_{\rm rs}c, \quad \frac{dR_{\rm cd}}{dt} = \beta_{\rm 3}c. \tag{22}$$

The FS velocity is determined by the shock jump conditions (Suzuki et al. 2017):

$$\beta_{\rm fs} = \frac{\hat{\gamma} \Gamma_3^2(-\beta_3)\beta_3 - (\hat{\gamma} - 1)(1 - \Gamma_3)}{\hat{\gamma} \Gamma_3^2(-\beta_3) - (\hat{\gamma} - 1)(-\Gamma_3\beta_3)},\tag{23}$$

where  $\hat{\gamma} = (4 + 1/\Gamma_3)/3$  is the effective adiabatic index of the shocked region. The RS velocity depends on the magnetization parameter and is given by

$$\beta_{\rm rs} = \frac{\beta_3 - \beta_{3\rm s}}{1 - \beta_3 \beta_{3\rm s}},\tag{24}$$

where  $\beta_{3s} = u_{3s}/\sqrt{1 + u_{3s}^2}$ .

## 2.2. Emission

In the pulsar wind nebula scenario, Region 3 corresponds to the shocked pulsar wind behind the RS. It is this region where the relativistic  $e^{\pm}$  pairs are heated and accelerated, thereby determining the injected electron distribution responsible for the subsequent radiation. The injection rate of electrons from Region 4 is assumed to follow a power-law distribution with an exponential cutoff (Kimura et al. 2019), expressed as

$$Q' = K \left(\frac{\gamma_{\rm e}'}{\gamma_{\rm m}'}\right)^{-p} \exp\left(-\frac{\gamma_{\rm e}'}{\gamma_{\rm max}'}\right),\tag{25}$$

where the normalization constant K is determined by

$$\int_{\gamma_{\rm m}'}^{\gamma_{\rm max}'} Q'(\gamma_{\rm e}', r) \, d\gamma_{\rm e}' = 4\pi R_{\rm rs}^2 n_4' \frac{\beta_4 - \beta_{\rm rs}}{1 - \beta_4 \beta_{\rm rs}} c. \tag{26}$$

Taking into account the relative velocity between the shock front and the fluid, the injection rate can be rewritten as

$$Q' = 4\pi R_{\rm rs}^2 n_4' (p-1) (\gamma_{\rm m}' - 1)^{p-1} (\gamma_{\rm e}' - 1)^{-p} \times \frac{\beta_4 - \beta_{\rm rs}}{1 - \beta_4 \beta_{\rm rs}} c \exp\left(-\frac{\gamma_{\rm e}'}{\gamma_{\rm max}'}\right), \tag{27}$$

where p=2.2 and  $\epsilon_{\rm e}=0.1$ . The minimum and maximum Lorentz factors of electrons are given by

$$\gamma'_{\rm m} = \epsilon_{\rm e} \frac{p-2}{p-1} (\Gamma_{34} - 1) f_{\rm a} + 1,$$
 (28)

and

$$\gamma'_{\text{max}} = \sqrt{\frac{3q_{\text{e}}B'}{4\sigma_{\text{T}}(U'_{\text{P}} + U'_{\text{e}})}},$$
 (29)

where  $\sigma_{\rm T}$  is the Thomson cross section,  $q_{\rm e}$  denote the electron charge,  $U_{\rm B}' = B'^2/(8\pi)$  is the magnetic energy density and  $U_{\rm s}'$  is the energy density of seed photons. Here, synchrotron

radiation and inverse Compton scattering are included as the cooling mechanisms that determine the maximum Lorentz factor.

The total comoving magnetic field B' is given by the sum of the comoving magnetic field in Region 3,  $B'_3$ , and the magnetic field generated in the RS region,  $B'_{rs}$ , i.e.,

$$B' = \sqrt{B_3^{'2} + B_{rs}^{'2}}. (30)$$

Here,  $B_3' = B_4'(4\Gamma_{34} + 3)f_b$ , and  $B_{rs}' = \sqrt{4\pi\epsilon_B(\Gamma_{34} - 1)f_an_3'm_ec^2}$ , where  $B_4' = \sqrt{4\pi n_4'm_ec^2\sigma}$  is the comoving magnetic field in Region 4 (the unshocked cold wind) (Liu et al. 2016),  $\epsilon_B = 0.1$  is the fraction of dissipated energy converted into magnetic fields, and  $m_e$  denotes the electron mass. The correction factor  $f_b$  is given by (Zhang & Kobayashi 2005; Mao et al. 2010)

$$f_{\rm b} = \frac{1}{4} \left[ 1 + \left( 1 + \frac{1}{u_{3\rm s}^2} \right)^{1/2} \right]. \tag{31}$$

The comoving electron number density in Region 4 is given by (Liu et al. 2016)

$$n_4' = \frac{\xi L_{\rm sd}}{4\pi R_{\rm rs}^2 \Gamma_4^2 m_{\rm e} c^3 (1+\sigma)},\tag{32}$$

where  $\xi=0.3$  is the conversion efficiency of spin-down luminosity into particle kinetic energy. Accordingly, the comoving electron number density in Region 3 is  $n_3'=(4\Gamma_{34}+3f_{\rm h})n_4'$  (Liu et al. 2016).

Assuming that the electron distribution  $N'_{\rm e}(\gamma'_{\rm e})$  reaches a steady state within the dissipation region, the continuity equation takes the form

$$\begin{cases} \frac{\partial}{\partial \gamma'_{e}} \left( -\frac{\gamma'_{e}}{t'_{cool}} N'_{e} \right) = Q', & \gamma'_{e} \geqslant \min(\gamma'_{m}, \gamma'_{c}), \\ N'_{e} = 0, & \gamma'_{e} < \min(\gamma'_{m}, \gamma'_{c}), \end{cases}$$
(33)

where the cooling Lorentz factor is

$$\gamma_{\rm c}' = \frac{3m_{\rm e}c}{4\sigma_{\rm T}\Gamma_{\rm 3}(U_{\rm B}' + U_{\rm s}')t}.$$
 (34)

The total cooling time in the comoving frame is defined as

$$t'_{\text{cool}} = (t'_{\text{syn}} + t'_{\text{eic}})^{-1},$$
 (35)

where  $t'_{\rm syn} = \gamma'_{\rm e}/\dot{\gamma}'_{\rm e,syn}$  is the synchrotron cooling time, and  $t'_{\rm eic} = \gamma'_{\rm e}/\dot{\gamma}'_{\rm e,eic}$  is the cooling time due to EIC scattering. The cooling rates of electrons due to synchrotron emission and EIC emission are given by

$$\dot{\gamma}'_{\rm e}$$
, syn =  $-\frac{3\sigma_{\rm T}\gamma'^{2}_{\rm e}B'^{2}}{12\pi m_{\rm e}C}$ , (36)

and

$$\dot{\gamma}'_{e}, \text{ eic} = -\frac{3\sigma_{T}}{4\gamma'^{2}_{e} m_{e} c} \int_{\nu'_{s,\text{min}}}^{\nu'_{s,\text{max}}} \frac{n'_{s}}{\nu'_{s}} d\nu'_{s}$$

$$\times \int_{\nu'_{\text{eic,min}}}^{\nu'_{\text{eic,max}}} F(q, g) h\nu'_{\text{eic}} d\nu'_{\text{eic}}, \tag{37}$$

where h is the Planck constant,  $n'_s$  is the comoving number density of seed photons,  $\nu'_s$  is the frequency of seed photons, and  $\nu'_{\rm eic}$  is the frequency of upscattered photons originating from the ejecta. The scattering function F(q, g) is expressed as

$$F(q, g) = \begin{cases} 2q \ln q + (1 + 2q)(1 - q) + \frac{(qg)^2}{2(1 + qg)}(1 - q), & 0 < q < 1, \\ 0, & \text{otherwise,} \end{cases}$$
(38)

with  $g = 4\gamma'_e h\nu'_s/(m_e c^2)$  and q = E/[g(1 - E)], where  $E = h\nu'_{\rm eic}/(\gamma'_e m_e c^2)$ . The integration limits for the upscattered photon energy are  $h\nu'_{\rm eic,min} = h\nu'_s$  and  $h\nu'_{\rm eic,max} = h\nu'_s \cdot [g/(g+1)]$ , h is the Planck constant.

The energy density of seed photons in the comoving frame of Region 3, after the thermal photons from the ejecta propagate back into this region, can be expressed as (Kimura et al. 2019)

$$U_{\rm s}' = \Gamma_{34} \frac{8\pi (h\nu_{\rm s}'/\Gamma_{34})^3}{h^3 c^3 [\exp(h\nu_{\rm s}'/(k_{\rm B}T'\Gamma_{34})) - 1]},$$
 (39)

where  $T' = [(E'_{\text{int},2} + E'_{\text{int},3})/(aV')]^{1/4}$  is the comoving temperature of the ejecta. The evolution of the comoving volume follows  $dV'/dt' = 4\pi R^2 \beta c$ . The number density of seed photons is then given by

$$n_{\rm s}' = \frac{U_{\rm s}'}{h\nu_{\rm s}'}.\tag{40}$$

The synchrotron emission power at a given comoving-frame frequency  $\nu' = \nu_{\rm obs}/(2\Gamma_{\rm 4})$  is given by (Sari et al. 1998; Li et al. 2021)

$$f'_{\text{syn}}(\nu', t_{\text{obs}}) = \frac{\sqrt{3} q_{\text{e}}^3 B'}{m_{\text{e}} c^2} \int_{\gamma'_{\text{e}}, \text{min}}^{\gamma'_{\text{e}}, \text{max}} N'_{\text{e}} F\left(\frac{\nu'}{\nu'_{\text{syn}}}\right) d\gamma'_{\text{e}}, \quad (41)$$

where  $F(x) = x \int_{x}^{+\infty} K_{5/3}(s) ds$  is the standard synchrotron kernel involving the modified Bessel function  $K_{5/3}$ , and the characteristic synchrotron frequency is  $\nu'_{\rm syn} = 3q_{\rm e}B'\gamma_{\rm e}^{'2}/(4\pi m_{\rm e}c)$ .

The EIC emission power at frequency  $\nu'_{\rm eic} = \nu_{\rm obs}/(2\Gamma_4)$  in the comoving frame is given by (Blumenthal & Gould 1970;

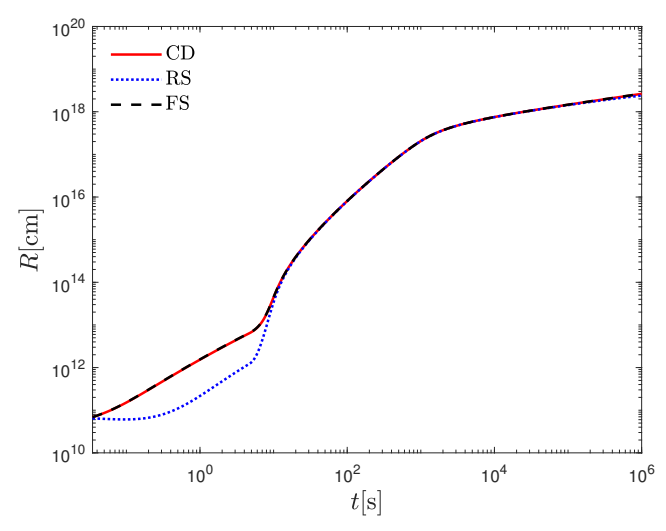


**Figure 1.** Time evolution of the positions of the contact discontinuity (red solid line), forward shock (black dashed line), and reverse shock (blue dotted line). Results are shown for  $M_{\rm ej}=1\times10^{-4}\,M_{\odot}$  and  $E_{\rm sd}=1\times10^{52}$  erg.

Zhang et al. 2019)

$$f'_{\text{eic}}(\nu'_{\text{eic}}, t_{\text{obs}}) = \frac{3\sigma_{\text{T}}ch\nu'_{\text{eic}}}{4}$$

$$\times \int_{\nu'_{\text{s,min}}}^{\nu'_{\text{s,max}}} \frac{n'_{\text{s}}}{\nu'_{\text{s}}} d\nu'_{\text{s}}$$

$$\times \int_{\nu'_{\text{s,min}}}^{\nu'_{\text{s,max}}} \frac{F(q, g)}{\gamma'_{\text{e}}^{2}} n'_{\text{e}} d\gamma'_{\text{e}}. \tag{42}$$

The optical depth of high-energy photons traveling through the ejecta in Region 2 is given by

$$\tau = \frac{\kappa_2 M_{\rm ej}}{4\pi R^2},\tag{43}$$

where  $M_{\rm ej}$  is the mass of the ejecta located ahead of the jet and the total opacity  $\kappa_2$  is modeled as

$$\kappa_2 = \kappa_0 \left( \frac{h\nu_s}{1 \text{ keV}} \right)^{-1},\tag{44}$$

with  $\kappa_0 = 7 \times 10^3 \, \text{cm}^2 \, \text{g}^{-1}$  describing the frequency-dependent absorption for X-ray photons (Ren & Dai 2022). Here, we take  $\kappa_2 = 0.5$  for optical photons.

The thermal luminosity from the ejecta at an observed frequency  $\nu$  can be calculated as (Yu et al. 2013)

$$F_{\text{th}}(t_{\text{obs}}) = \frac{1}{\max(\tau, 1)} \cdot \frac{8\pi^2 \mathcal{D}^2 R^2}{h^3 c^2} \cdot \frac{(h\nu'/\mathcal{D})^4}{\exp(h\nu'/(\mathcal{D}k_{\text{B}}T')) - 1},$$
(45)

where  $\mathcal{D} = [\Gamma(1 - \beta(t))]^{-1}$  is the Doppler factor.

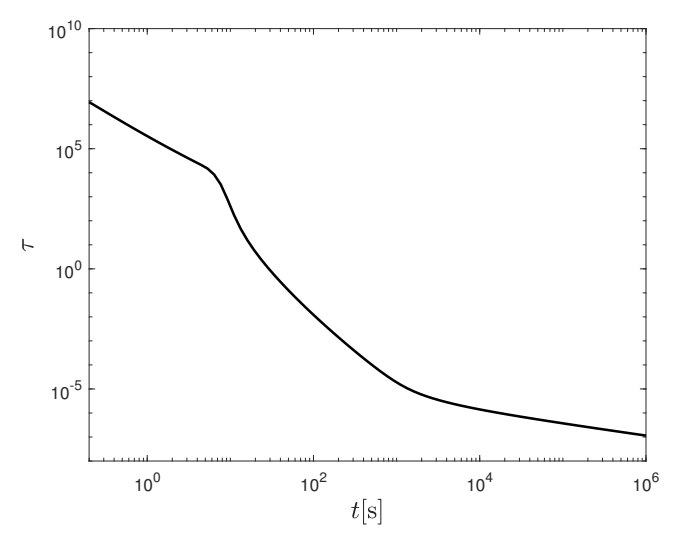


**Figure 2.** Time evolution of the optical depth of the ejecta for the case of  $E_{\rm sd} = 1 \times 10^{52}$  erg and  $M_{\rm ej} = 1 \times 10^{-4} \, M_{\odot}$ .

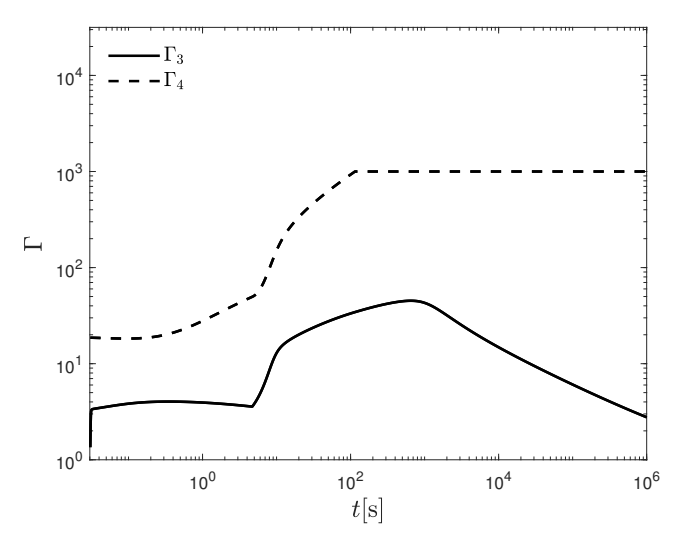


**Figure 3.** Time evolution of the Lorentz factors in Regions 3 and 4, for  $E_{\rm sd}=1\times 10^{52}\,{\rm erg}$  and  $M_{\rm ej}=1\times 10^{-4}\,M_{\odot}$ . The solid and dashed lines correspond to Regions 3 and 4, respectively.

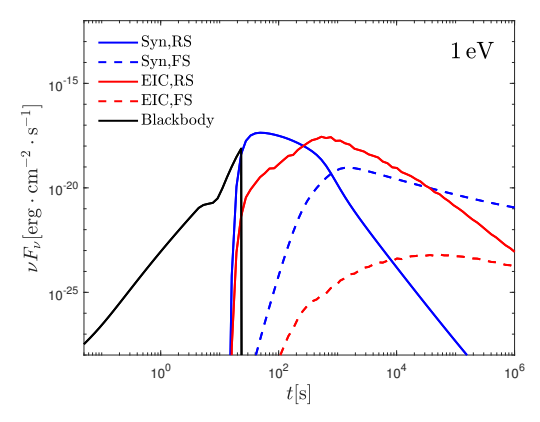
Finally, the total non-thermal radiation observed flux at frequency  $\nu_{\rm obs}$  is given by (Li et al. 2024)

$$F_{\nu_{\text{obs}}}(t_{\text{obs}}) = \frac{\Gamma_4 (f'_{\text{syn}} + f'_{\text{eic}})(1+z) e^{-\tau}}{4\pi d_{\text{L}}^2},$$
 (46)

where  $d_{\rm L} = 40 \, {\rm Mpc}$  is the adopted luminosity distance.

The calculation of the FS follows the same procedure as that of the RS, except for the differences in the injected electron population and the comoving magnetic field. The electron injection rate in the FS region is given by

$$Q_{\rm fs}' = 4\pi R_{\rm fs}^2 n_1'(p-1)(\gamma_{\rm m,fs}' - 1)^{p-1}(\gamma_{\rm e}' - 1)^{-p}, \qquad (47)$$



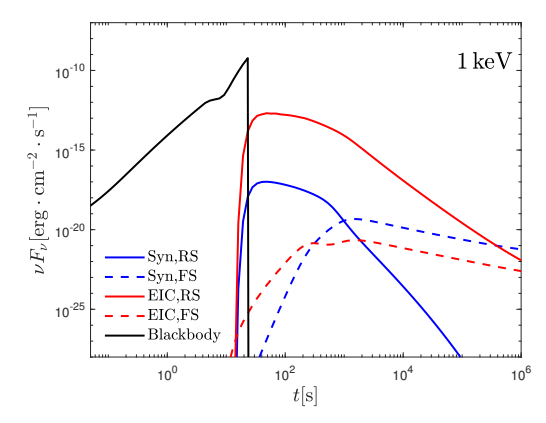


Figure 4. Light curves in different energy bands. In both panels, the solid lines represent emission from the reverse shock, while the dashed lines represent emission from the forward shock. Different radiation mechanisms are shown in different colors. The left panel shows the light curve in the 1 eV energy band, and the right panel shows that in the 1 keV band. The light curves are computed with  $E_{\rm sd} = 1 \times 10^{52}$  erg and  $M_{\rm ej} = 1 \times 10^{-4} M_{\odot}$ .

and the corresponding comoving magnetic field is

$$B_{\rm fs}' = \sqrt{32\pi\epsilon_{\rm B}n_{\rm ISM}'m_{\rm p}} \Gamma_{\rm 3}c, \tag{48}$$

where  $R_{\rm fs}$  denotes the radius of the FS,  $m_{\rm p}$  is the proton mass.

#### 3. Results

The merger of a BNS system can result in the formation of a rapidly rotating and highly magnetized neutron star, accompanied by significant mass ejection. The newborn magnetar releases magnetic dipole energy, driving a Poynting-fluxdominated jet that interacts with the ejecta, leading to the formation of forward and reverse shocks. We compute the positions of the CD, FS, and RS using Equation (18), and present the results in Figure 1. The calculation is performed for an ejecta mass of  $M_{\rm ej}=1\times 10^{-4}\,M_{\odot}$  and a spin-down energy of  $E_{\rm sd}=1\times 10^{52}\,{\rm erg}$ . As shown in Figure 1, when the Poynting flux first collides with the ejecta, the RS propagates slightly backward relative to the flow direction. Subsequently, the RS lags far behind both the CD and the FS until the FS crosses the ejecta and enters the ISM. At this stage, the RS gradually catches up with the CD and the FS, and eventually the three nearly coincide in the ISM. It should be noted that when the ejecta mass is sufficiently large ( $M_{\rm ej} > 3$   $\times$  $10^{-4} M_{\odot}$ ), the RS propagates inward rapidly and eventually vanishes. For a typical BNS merger, however, the ejecta mass along the jet direction is about  $10^{-4} M_{\odot}$  (Ren et al. 2020). Therefore, in the following radiation calculations, we only consider the case where the RS persists.

Next, we compute the time evolution of the optical depth using Equation (39). Figure 2 shows that the optical depth drops below unity at around  $t \sim 60 \, \mathrm{s}$ . This implies that before this time, the radiation from the RS is trapped within the ejecta and cannot escape. Consequently, the early-time emission is dominated by thermal (blackbody) radiation from the ejecta. Using Equations (4) and (9), we also calculate the time evolution of the Lorentz factors in Regions 3 and 4 in Figure 3.

Figure 3 illustrates that the Lorentz factor of Region 4 increases until it reaches a saturation stage. During the energy injection phase, the ejecta is gradually accelerated by the injected jet energy and subsequently decelerated by the interaction with the external medium once the spin-down energy injection becomes ineffective.

Finally, in Figure 4 we present the model light curves in the  $1 \, \mathrm{eV}$  and  $1 \, \mathrm{keV}$  energy bands for  $E_{\mathrm{sd}} = 1 \times 10^{52} \, \mathrm{erg}$  and  $M_{\mathrm{ej}} = 1 \times 10^{-4} \, M_{\odot}$ . Note that the calculation of blackbody radiation is terminated once the ejecta becomes optically thin. In the  $1 \, \mathrm{eV}$  band, the early emission is dominated by blackbody radiation from the ejecta. After the ejecta becomes optically thin, synchrotron emission from the RS dominates, followed at later times by EIC emission from the RS. Eventually, synchrotron emission from the FS becomes the primary contribution. In the  $1 \, \mathrm{keV}$  band, the early emission is likewise dominated by blackbody radiation from the ejecta. However, once the ejecta becomes optically thin, the EIC emission from the RS provides the main contribution to the observed flux.

## 4. Summary and Conclusion

This study investigates the dynamical evolution and radiation mechanisms of a PWN powered by a magnetar central engine. In particular, we consider the time-dependent evolution of the magnetization parameter, as well as the EIC process in which seed photons from the ejecta are upscattered by electrons in the RS. The main conclusions are summarized as follows:

First, when the Poynting flux initially collides with the ejecta, if the ejecta mass is sufficiently large  $(M_{\rm ej} > 3 \times 10^{-4}\,M_{\odot})$ , the RS rapidly propagates inward and eventually disappears. For smaller ejecta masses, the RS propagates slightly backward relative to the flow direction. Subsequently, the RS falls far behind both the CD and the FS until the FS traverses the ejecta and enters the ISM. At this

stage, the RS gradually catches up with the CD and the FS, and the three nearly coincide in the ISM at late times. Second, during the energy injection phase, the ejecta is gradually accelerated by the injected jet energy and later decelerated by interaction with the external medium once the spin-down energy input ceases to be effective. Finally, during the early optically thick stage, the emission is dominated by blackbody radiation from the ejecta. After the system becomes optically thin, EIC emission from the RS dominates the 1 keV band. In contrast, in the 1 eV band, synchrotron emission from the RS dominates shortly after transparency, while EIC emission becomes the leading component at later times.

## Acknowledgments

We thank the anonymous referee for helpful feedback on the manuscript. This work is supported by the National Natural Science Foundation of China (grant Nos. 12273005, 12494575, and 12133003), the National Key R&D Program of China (grant Nos. 2023YFE0117200 and 2024YFA1611700), the special funding for Guangxi Bagui Youth Scholars, and the Guangxi Talent Program ("Highland of Innovation Talents").

## References

```
Abbott, B. P., Abbott, R., Abbott, T. D., et al. 2017a, PhRvL, 119, 161101 Abbott, B. P., Abbott, R., Abbott, T. D., et al. 2017b, ApJL, 848, L12 Acernese, F., Agathos, M., Agatsuma, K., et al. 2015, CQGra, 32, 024001 Barthelmy, S. D., Chincarini, G., Burrows, D. N., et al. 2005, Natur, 438, 994 Bartos, I., Brady, P., & Márka, S. 2013, CQGra, 30, 123001 Beniamini, P., & Giannios, D. 2017, MNRAS, 468, 3202 Blumenthal, G. R., & Gould, R. J. 1970, RvMP, 42, 237 Chevalier, R. A., & Fransson, C. 1992, ApJ, 395, 540 Coroniti, F. V. 1990, ApJ, 349, 538 Dai, Z. G. 2004, ApJ, 606, 1000 Dai, Z. G., & Liu, R.-Y. 2012, ApJ, 759, 58 Dai, Z. G., & Lu, T. 1998a, PhRvL, 81, 4301 Dai, Z. G., & Lu, T. 1998b, A&A, 333, L87 Dai, Z. G., Wang, X. Y., Wu, X. F., & Zhang, B. 2006, Sci, 311, 1127 Drenkhahn, G., & Spruit, H. C. 2002, A&A, 391, 1141
```

```
Duncan, R. C., & Thompson, C. 1992, ApJL, 392, L9
Eichler, D., Livio, M., Piran, T., & Schramm, D. N. 1989, Natur, 340, 126
Fan, Y. Z., Wei, D. M., & Wang, C. F. 2004, A&A, 424, 477
Fox, D. B., Frail, D. A., Price, P. A., et al. 2005, Natur, 437, 845
Gaensler, B. M., & Slane, P. O. 2006, ARA&A, 44, 17
Gao, H., Ding, X., Wu, X.-F., Dai, Z.-G., & Zhang, B. 2015, ApJ, 807, 163
Gao, H., Ding, X., Wu, X.-F., Zhang, B., & Dai, Z.-G. 2013, ApJ, 771, 86
Giacomazzo, B., & Perna, R. 2013, ApJL, 771, L26
Gompertz, B. P., O'Brien, P. T., & Wynn, G. A. 2014, MNRAS, 438, 240
Harry, G. M. & LIGO Scientific Collaboration. 2010, CQGra, 27, 084006
Kimura, S. S., Murase, K., Ioka, K., et al. 2019, ApJL, 887, L16
Kotera, K., Phinney, E. S., & Olinto, A. V. 2013, MNRAS, 432, 3228
Li, L.-X., & Paczyński, B. 1998, ApJL, 507, L59
Li, S.-Z., & Yu, Y.-W. 2016, ApJ, 819, 120
Li, X.-Y., Lin, D.-B., Ren, J., et al. 2021, ApJ, 922, 22
Li, Y.-F., Lin, D.-B., Ren, J., et al. 2024, ApJ, 960, 17
Li, Y.-P., Chen, Z.-L., Lin, D.-B., & Liang, E.-W. 2024, ApJ, 968, 104
Li, Y.-P., Lin, D.-B., Li, G.-Y., Zhou, Z.-M., & Liang, E.-W. 2025, ApJ,
Liu, L. D., Wang, L. J., & Dai, Z. G. 2016, A&A, 592, A92
Mao, Z., Yu, Y. W., Dai, Z. G., Pi, C. M., & Zheng, X. P. 2010, A&A,
   518, A27
Michel, F. C. 1994, ApJ, 431, 397
Nava, L., Sironi, L., Ghisellini, G., Celotti, A., & Ghirlanda, G. 2013,
   MNRAS, 433, 2107
Paczynski, B. 1986, ApJL, 308, L43
Ren, J., & Dai, Z. G. 2022, MNRAS, 512, 5572
Ren, J., Lin, D.-B., Zhang, L.-L., et al. 2020, ApJL, 901, L26
Rezzolla, L., Giacomazzo, B., Baiotti, L., et al. 2011, ApJL, 732, L6
Rowlinson, A., O'Brien, P. T., Metzger, B. D., Tanvir, N. R., & Levan, A. J.
   2013, MNRAS, 430, 1061
Rowlinson, A., O'Brien, P. T., Tanvir, N. R., et al. 2010, MNRAS, 409, 531
Sari, R., Piran, T., & Narayan, R. 1998, ApJL, 497, L17
Siegel, D. M., & Ciolfi, R. 2016a, ApJ, 819, 14
Siegel, D. M., & Ciolfi, R. 2016b, ApJ, 819, 15
Somiya, K. 2012, CQGra, 29, 124007
Suzuki, A., Maeda, K., & Shigeyama, T. 2017, ApJ, 834, 32
Wang, L.-J., & Dai, Z.-G. 2013, ApJL, 774, L33
Wang, L.-J., Dai, Z.-G., & Yu, Y.-W. 2015, ApJ, 800, 79
Wu, X.-F., Gao, H., Ding, X., et al. 2014, ApJL, 781, L10
Yu, Y. W., & Dai, Z. G. 2007, A&A, 470, 119
Yu, Y.-W., Li, S.-Z., & Dai, Z.-G. 2015, ApJL, 806, L6
Yu, Y.-W., Zhang, B., & Gao, H. 2013, ApJL, 776, L40
Zhang, B. 2013, ApJL, 763, L22
Zhang, B., & Kobayashi, S. 2005, ApJ, 628, 315
Zhang, B., & Mészáros, P. 2001, ApJL, 552, L35
Zhang, Y., Geng, J.-J., & Huang, Y.-F. 2019, ApJ, 877, 89
```